Available online at www.sciencedirect.com
SCIENCE DIRECT®
Journal of Computational Physics 215 (2006) 526–551
JOURNAL OF COMPUTATIONAL PHYSICS
www.elsevier.com/locate/jcp

Compressible large eddy simulations of wall-bounded turbulent flows using a semi-implicit numerical scheme for low Mach number aeroacoustics

Jungsoo Suh, Steven H. Frankel *, Luc Mongeau, Michael W. Plesniak

School of Mechanical Engineering, Purdue University, West Lafayette, IN 47907-2088, USA

Received 11 June 2005; received in revised form 19 September 2005; accepted 31 October 2005
Available online 5 January 2006

Abstract

Large eddy simulations (LES) of low-speed, wall-bounded turbulent flows were conducted by numerically integrating the compressible Navier–Stokes equations in a generalized curvilinear coordinate system. An efficient numerical scheme based on a third-order additive semi-implicit Runge–Kutta method for time advancement and a sixth-order accurate, compact finite-difference scheme for spatial discretization were used. The convective terms in the wall-normal direction were treated implicitly to remove the time-step limitation associated with the use of fine meshes in the near-wall region for high Reynolds number viscous flows. The dynamic Smagorinsky subgrid-scale eddy viscosity model was used to close the filtered equations. Generalized characteristic-based non-reflecting boundary conditions were used together with grid stretching and enhanced damping in the exit zone. The accuracy and efficiency of the numerical scheme was assessed by simple acoustic model problems and by comparing LES predictions for fully developed turbulent channel flow and turbulent separated flow in an asymmetric diffuser to previous direct numerical simulation (DNS) and experimental data, respectively. LES predictions for both flows were in reasonable agreement with the DNS and experimental mean velocity and turbulence statistics. The findings suggest that the numerical approach employed here offers comparable accuracy to similar recent studies at approximately one-third of the computational cost and may provide both an accurate and efficient way to conduct computational aeroacoustics studies for low Mach number, confined turbulent flows.

Keywords: LES; Turbulence; Wall-bounded flows; Semi-implicit scheme

1. Introduction

One challenge of efficient, direct computation of sound radiation from low Mach number turbulent flows is to relax the CFL restriction related to acoustic waves, while minimizing the amount of numerical dissipation

* Corresponding author.
E-mail address: frankel@ecn.purdue.edu (S.H. Frankel).

0021-9991/$ - see front matter © 2005 Elsevier Inc. All rights reserved.
doi:10.1016/j.jcp.2005.10.036

Nomenclature

C	eddy viscosity model constant
c	speed of sound
C_f	skin friction coefficient
C_p	constant pressure specific heat
C_v	constant volume specific heat
$\mathbf{E}$, $\mathbf{F}$, $\mathbf{G}$	inviscid flux vectors
$\mathbf{E}_v$, $\mathbf{F}_v$, $\mathbf{G}_v$	viscous flux vectors
e_t	specific total energy
$\mathbf{f}$	spatial discretization of non-stiff terms
f	arbitrary variable
$\bar{f}$	large-scale component of variable f
f''	small-scale component of variable f
$\tilde{f}$	Favre-average of variable f
$\hat{f}$	test-filtered variable f
$\bar{f}(z)$	variable f averaged over homogeneous spatial plane and time
$G(\mathbf{x}-\mathbf{y},\Delta)$	filter function
$\mathbf{g}$	spatial discretization of stiff terms
H	inlet height
$\mathbf{I}$	identity matrix
J	Jacobian of coordinate transformation
$\mathbf{J}$	Jacobian matrix of stiff term in semi-implicit scheme
$\mathbf{k}$	increment of discretized flow field variable vector
L_i	amplitude of characteristic wave
L^*	newly updated amplitude of characteristics
M	Mach number
p	pressure
Pr	Prandtl number
Pr_t	turbulent Prandtl number
Q	second invariant of velocity gradient tensor
$\mathbf{Q}$	vector of dependent variables
$\mathcal{Q}_i$	subgrid-scale heat flux
q_i	heat transfer flux vector
Re	Reynolds number
$\mathbf{S}$	source term for channel flow computation
$\mathbf{S}_v$	source term from the viscous flux vectors
S_{ij}	symmetric part of velocity gradient tensor
T	temperature
T_{ij}	Lighthill source tensor
t	time
U_b	bulk velocity
U_c	centerline velocity
$\mathbf{u}$	discretized flow field variable vector
u, v, w	Cartesian velocity components
u_i	alternate notation for (u,v,w)
u_τ	friction velocity
$\mathbf{v}$	velocity vector
(x,y,z)	Cartesian coordinates
x_i	alternate notation for (x,y,z)
δ	half-height of inlet

δ_{ij}	Kronecker delta
γ	specific heat ratio
κ	von Karman constant
λ_i	characteristic velocity of characteristic wave
μ	dynamic viscosity
ν	kinematic viscosity
Θ	dilatation
ρ	density
σ_{ij}	stress tensor
τ_{ij}	subgrid-scale stress tensor
Ω_{ij}	antisymmetric part of velocity gradient tensor
(ξ,η,ζ)	computational coordinates
Δ	grid-filter width
$\hat{\Delta}$	test-filter width
$\langle\,\rangle$	spatial averaging operator

in the numerical schemes. The solution of the incompressible form of the Navier–Stokes equations (NSE) is advantageous for low Mach number flow simulations. Because the time-step size is only limited by the convective velocity, and not the acoustic velocity. This reduces computational times significantly, but removes acoustic waves from the system. In the field of computational aeroacoustics (CAA), the direct computation of both the unsteady flow and the sound generated by it requires the use of the compressible form of the NSE [1]. In many CAA applications to date, explicit numerical schemes, such as Runge–Kutta methods, have been used to integrate the semi-discrete form of the compressible NSE in order to provide a better resolution of acoustic waves. Unfortunately, the resulting system of ordinary differential equations (ODE) is stiff due to the wide range of eigenvalues, implying severe CFL-based time-step restrictions based on the sum of the acoustic and convective velocities. This is particularly troublesome for simulating three-dimensional, wall-bounded turbulent flows designed to address aeroacoustics issues, as these are already computationally expensive due to fine near-wall meshes. Hence, many CAA studies have been limited to unconfined flows, such as jets, cavities, and airfoil trailing edges [1]. The issue of direct computation of sound from confined turbulent flows has received relatively little attention in the open literature.

Implicit numerical schemes can reduce the time-step limitation imposed by the CFL condition, but this is often at the price of increased numerical dissipation of acoustic waves [2]. There are a number of other approaches designed to avoid the CFL condition that are based on modifying the compressible NSE [2]. These include splitting the NSE [3], extending the pressure-correction approach to compressible flows [4], or utilizing a preconditioning matrix to accelerate convergence [5,6]. While improving low-Mach number flow computational efficiency, these algorithms are not time-accurate. They are typically designed for steady flows applications, and often feature significant artificial damping. Their time accuracy can be addressed through dual time-stepping, but implementation has usually been limited to second-order accuracy [7]. In addition, since this approach modifies the governing equations, non-reflecting boundary conditions must be reformulated. Recently Wall et al. [2] developed a semi-implicit algorithm to suppress high-frequency acoustic waves based on a staggered-grid, second-order, pressure-correction method. For applications where low-frequency acoustics dominate, such as combustion instability, this may be a viable approach. High-order compact finite-difference schemes [8] are commonly used for spatial discretization in CAA studies due to their improved accuracy and efficiency as compared to low-order methods [1,9]. Hence, it is desirable to combine a high-order accurate spatial scheme with a time-stepping scheme that can efficiently capture acoustic waves at low Mach number.

Motivated by the above reason, this study combines a third-order, additive, semi-implicit Runge–Kutta (ASIRK) time-stepping scheme, developed by Zhong [10], with a sixth-order accurate compact finite-difference spatial scheme [8]. Due to fine grid spacing in the near-wall region of viscous flows or when dealing with fast thermochemistry, small time steps are needed when using an explicit time integration scheme, making the

equations stiff. In the semi-implicit approach, stiff terms in the governing equations are treated implicitly to remove the stability restriction, whereas non-stiff terms are treated explicitly. In the reacting flow problem studied by Zhong [11], the stiff thermochemical source terms were treated implicitly. In our wall-bounded turbulent viscous flow problem, the convective transport terms in the wall-normal direction are treated implicitly, with all other terms treated explicitly.

Hence, acoustic wave resolution in the primary flow and sound propagation directions is achieved, with minimal numerical diffusion effects associated with the implicit scheme in the wall-normal direction, where physical damping effects are already present. In addition, wall boundary conditions are developed to ensure implicit advancement of the equations to avoid time-step limitations associated with the use of a fine near-wall mesh. Dong and Zhong [12] performed a similar study, treating all terms in the wall-normal direction implicitly and all other terms explicitly. However, they used explicit centered finite-differencing schemes, which are known to be less accurate than compact schemes for spatial descritization, and they did not discuss the handling of boundary conditions associated with the implicit scheme in detail.

In the present study, the ASIRK scheme is used to conduct large eddy simulation (LES) studies of low Mach number, wall-bounded turbulent flows based on integrating the compressible NSE. In the past few years, the application of LES to CAA problems has grown [1]. This is because of its ability to simulate large-scale turbulent flow dynamics at higher Reynolds number and for more complex geometries than direct numerical simulations (DNS) for the same or lesser grid size. More accurate flow predictions and more insight into the nature of acoustic sources are two advantages of LES over Reynolds-averaged Navier–Stokes (RANS) approaches in CAA. In this study, LES predictions are compared to previous computed or measured results for fully developed turbulent channel flow and separated flow in a planar asymmetric diffuser. The channel flow results will also be used to generate turbulent inlet conditions for the diffuser simulations. The goal of this paper is flow-field validation as a first step towards efficient CAA of wall-bounded turbulent flows.

Fully developed turbulent channel flows are widely used as a benchmark due to their geometrical simplicity and well-defined boundary conditions. There exists a large number of published DNS and LES studies based on solving the incompressible NSE. The first reliable results featuring full resolution of the near-wall region were obtained by Moin and Kim [13] using the Smagorinsky subgrid-scale (SGS) model. Higher Reynolds number simulations, performed by Piomelli [14], used the dynamic Smagorinsky SGS model. More recent studies showed that improved accuracy could be obtained using the approximate deconvolution model [15]. Only a few studies have featured the use of the compressible flow equations for turbulent channel flow. Okong and Knight [16] employed an unstructured finite volume approach for LES of compressible turbulent channel flows using the Smagorinsky SGS model and obtained reasonable results. Lenormand et al. [17] tested two kinds of subgrid-scale models for both subsonic and supersonic compressible channel flows and found their mixed-scale model yields better results for mean flow quantities than the Smagorinsky model. Most recently Rizzetta et al. [18] conducted LES of low-Mach number turbulent channel flows by solving the compressible flow equations using high-order compact finite-difference scheme with high-order implicit filters and achieved reasonable results.

Turbulent flow through a diffuser introduces the added complication of an adverse pressure gradient and the potential for flow separation. Obi et al. [19] conducted wind tunnel experiments of flow through a planar asymmetric diffuser, where a very high aspect ratio of the diffuser inlet (1:35) was used to try to maintain two-dimensional flow. Pressure measurements were made along the flat wall and LDA was used to obtain mean velocity and Reynolds stress profiles. However, their experiment had several deficiencies associated with mass conservation due to three-dimensional effects. Buice and Eaton [20] carefully re-created the experiment by Obi et al. using the novel control of sidewall boundary layer leakage and measured mean velocity, Reynolds stress, skin friction, and pressure at several locations providing a valuable data base for model validation studies [21].

RANS predictions reported by Obi et al. [19] showed that the standard k–ϵ model failed to predict the extent of the separation inside the diffuser, and only slight improvement was obtained with a second-moment closure. Durbin [22] successfully predicted the mean velocity, turbulence intensity, and diffuser recirculation zone in the Obi experiment using his k–ϵ–v^2 model. A comparative assessment of several turbulence models, conducted using commercial CFD codes, confirmed Durbin's findings [23]. Apsley and

Leschziner [24] tested linear and non-linear eddy-viscosity models, as well as Reynolds stress models, and found no model was able to correctly resolve the flow near the corner of the deflected wall and highlighted problems associated with the "flapping" motion of the unsteady separation region. Recently, Gullan-Strand et al. [25] found that the turbulent kinetic energy dissipation rate associated with their explicit algebraic Reynolds stress model was overestimated. Kaltenbach et al. [21] obtained LES predictions for mean flow profiles and coefficients that were in excellent agreement with the experimental data of Buice and Eaton [20]. Their simulations highlighted flow prediction sensitivity to inlet conditions, for which they employed an auxiliary turbulent channel flow simulation. They also found the dynamics SGS model they used provided a significant contribution to the total dissipation rate in their turbulent kinetic energy budget analysis.

The rest of the paper is organized as follows. The next two sections provide detailed descriptions of the mathematical equations and numerical methods, respectively. Following this, results from simple test cases followed by comparisons of LES predictions to previous DNS and experimental data are presented. A brief summary and conclusion section ends the paper.

2. Mathematical formulation

2.1. Governing equations

The governing equations under consideration here are the unsteady, three-dimensional, compressible, Favre-filtered, Navier–Stokes equations, written below in non-dimensional, conservative form for a generalized curvilinear coordinate system:

$$\frac{\partial \hat{\mathbf{Q}}}{\partial t}+\frac{\partial \hat{\mathbf{E}}}{\partial \xi}+\frac{\partial \hat{\mathbf{F}}}{\partial \eta}+\frac{\partial \hat{\mathbf{G}}}{\partial \zeta}=\mathbf{S}_{\mathrm{v}}+\mathbf{S}, \tag{1}$$

where t is time, and ξ, η, and ζ are the coordinates of the uniformly spaced computational domain. Here, $\hat{\mathbf{Q}}$ is the vector of dependent variables, $\hat{\mathbf{E}}$, $\hat{\mathbf{F}}$, and $\hat{\mathbf{G}}$ are the inviscid flux vectors, $\mathbf{S}_{\mathrm{v}}$ is the source term from the viscous flux vectors, and $\mathbf{S}$ is a vector source term that is non-zero only for the channel flow computations.

The filtered form of an arbitrary flow property f is given by the convolution integral:

$$\bar{f}(\mathbf{x})=\int_D G(\mathbf{x}-\mathbf{y},\Delta)f(\mathbf{y})\,\mathrm{d}\mathbf{y}, \tag{2}$$

where G is the filter function, Δ is the filter width, and D implies the entire computational domain. The filters used in this study will be discussed in Section 3. This allows f to be decomposed into its large-scale ($\bar{f}$) and subgrid-scale (f'') components

$$f=\bar{f}+f''. \tag{3}$$

In compressible flow, it is customary to use Favre-averaged flow properties defined as:

$$\tilde{f}=\frac{\overline{\rho f}}{\bar{\rho}}. \tag{4}$$

The vector of dependent variables in Eq. (1) is given as:

$$\hat{\mathbf{Q}}=\frac{1}{J}\mathbf{Q}=\frac{1}{J}\begin{bmatrix}\bar{\rho}\\ \bar{\rho}\tilde{u}\\ \bar{\rho}\tilde{v}\\ \bar{\rho}\tilde{w}\\ \bar{\rho}\tilde{e}_{\mathrm{t}}\end{bmatrix}, \tag{5}$$

where u, v, w are the Cartesian velocity components representing here streamwise, spanwise, and normal velocity components, respectively, J is the Jacobian of the coordinate transformation, ρ is the density, p is the pressure, and e_{t} is the specific total energy defined as:

$$\tilde{e}_t = \frac{1}{2}\bar{\rho}\tilde{u}_k\tilde{u}_k + \frac{1}{\gamma}\bar{p}, \tag{6}$$

where the specific heat ratio, $\gamma = \frac{C_p}{C_v}$ (1.4 for air), corresponds to an ideal, calorically perfect gas with constant specific heats and implies the following state equation:

$$\bar{p} = \frac{\bar{\rho}\tilde{T}}{\gamma M_\infty^2}, \tag{7}$$

where T is the temperature and M_∞ is the reference Mach number. The inviscid flux vectors in the generalized coordinates are given by:

$$\hat{\mathbf{E}} = (1/J)(\xi_x\mathbf{E} + \xi_y\mathbf{F} + \xi_z\mathbf{G}), \tag{8}$$

$$\hat{\mathbf{F}} = (1/J)(\eta_x\mathbf{E} + \eta_y\mathbf{F} + \eta_z\mathbf{G}), \tag{9}$$

$$\hat{\mathbf{G}} = (1/J)(\zeta_x\mathbf{E} + \zeta_y\mathbf{F} + \zeta_z\mathbf{G}), \tag{10}$$

where **E**, **F**, and **G** are defined as:

$$\mathbf{E} = \begin{bmatrix} \bar{\rho}\tilde{u} \\ \bar{\rho}\tilde{u}^2 + \bar{p} \\ \bar{\rho}\tilde{u}\tilde{v} \\ \bar{\rho}\tilde{u}\tilde{w} \\ (\bar{\rho}\tilde{e}_t + \bar{p})\tilde{u} \end{bmatrix}, \tag{11}$$

$$\mathbf{F} = \begin{bmatrix} \bar{\rho}\tilde{v} \\ \bar{\rho}\tilde{u}\tilde{v} \\ \bar{\rho}\tilde{v}^2 + \bar{p} \\ \bar{\rho}\tilde{v}\tilde{w} \\ (\bar{\rho}\tilde{e}_t + \bar{p})\tilde{v} \end{bmatrix}, \tag{12}$$

$$\mathbf{G} = \begin{bmatrix} \bar{\rho}\tilde{w} \\ \bar{\rho}\tilde{u}\tilde{w} \\ \bar{\rho}\tilde{v}\tilde{w} \\ \bar{\rho}\tilde{w}^2 + \bar{p} \\ (\bar{\rho}\tilde{e}_t + \bar{p})\tilde{w} \end{bmatrix}. \tag{13}$$

The source term $\mathbf{S}_v$ represents the sum of viscous flux vector derivatives:

$$\mathbf{S}_v = \frac{\partial\hat{\mathbf{E}}_v}{\partial\xi} + \frac{\partial\hat{\mathbf{F}}_v}{\partial\eta} + \frac{\partial\hat{\mathbf{G}}_v}{\partial\zeta}. \tag{14}$$

These viscous flux vectors are defined by:

$$\hat{\mathbf{E}}_v = (1/J)(\xi_x\mathbf{E}_v + \xi_y\mathbf{F}_v + \xi_z\mathbf{G}_v), \tag{15}$$

$$\hat{\mathbf{F}}_v = (1/J)(\eta_x\mathbf{E}_v + \eta_y\mathbf{F}_v + \eta_z\mathbf{G}_v), \tag{16}$$

$$\hat{\mathbf{G}}_v = (1/J)(\zeta_x\mathbf{E}_v + \zeta_y\mathbf{F}_v + \zeta_z\mathbf{G}_v), \tag{17}$$

where $\mathbf{E}_v$, $\mathbf{F}_v$,$\mathbf{G}_v$ are defined by:

$$\mathbf{E}_v = \begin{bmatrix} 0 \\ \tilde{\sigma}_{11} + \tau_{11} \\ \tilde{\sigma}_{12} + \tau_{12} \\ \tilde{\sigma}_{13} + \tau_{13} \\ \tilde{u}_i\tilde{\sigma}_{1i} + \tilde{q}_1 + \mathscr{Q}_1 \end{bmatrix}, \tag{18}$$

$$\mathbf{F}_v = \begin{bmatrix} 0 \\ \tilde{\sigma}_{21} + \tau_{21} \\ \tilde{\sigma}_{22} + \tau_{22} \\ \tilde{\sigma}_{23} + \tau_{23} \\ \tilde{u}_i\tilde{\sigma}_{2i} + \tilde{q}_2 + \mathscr{Q}_2 \end{bmatrix}, \tag{19}$$

$$\mathbf{G}_v = \begin{bmatrix} 0 \\ \tilde{\sigma}_{31} + \tau_{31} \\ \tilde{\sigma}_{32} + \tau_{32} \\ \tilde{\sigma}_{33} + \tau_{33} \\ \tilde{u}_i\tilde{\sigma}_{3i} + \tilde{q}_3 + \mathscr{Q}_3 \end{bmatrix}, \tag{20}$$

respectively. Components of the stress tensor and the heat transfer flux vector are expressed as:

$$\tilde{\sigma}_{ij} = \frac{\tilde{\mu}}{Re}\left(\frac{\partial \tilde{u}_i}{\partial x_j} + \frac{\partial \tilde{u}_j}{\partial x_i} - \frac{2}{3}\delta_{ij}\frac{\partial \tilde{u}_k}{\partial x_k}\right), \tag{21}$$

$$\tilde{q}_i = \left[\frac{1}{(\gamma-1)M_\infty^2}\right]\left(\frac{\tilde{\mu}}{RePr}\right)\frac{\partial \tilde{T}}{\partial x_i}, \tag{22}$$

where $\tilde{\mu}$ is the non-dimensionalized dynamic viscosity, Re is the Reynolds number, and Pr is the Prandtl number. The non-dimensional viscosity μ and Pr are assumed constant with values of 1 and 0.7, respectively. The corresponding SGS stress tensor and heat flux vectors are given as:

$$\tau_{ij} = \bar{\rho}(\tilde{u}_i\tilde{u}_j - \widetilde{u_iu_j}), \tag{23}$$

$$\mathscr{Q}_i = \bar{\rho}(\tilde{u}_i\tilde{T} - \widetilde{u_iT}). \tag{24}$$

Note that the pressure and temperature dilatation correlation terms in the filtered energy equation have been neglected due to the low Mach number of the flows considered here [26].

2.2. SGS turbulence model

The dynamic Smagorinsky SGS model, first proposed by Germano et al. [27] for incompressible flows and later extended by Moin et al. [28] for compressible flows, is used here. The compressible version of the model in trace-free form is given as

$$\tau_{ij} - \frac{1}{3}\tau_{kk}\delta_{ij} = -2C\bar{\rho}\Delta^2|\tilde{S}|\left(\tilde{S}_{ij} - \frac{1}{3}\tilde{S}_{kk}\delta_{ij}\right), \tag{25}$$

where $\tilde{S}_{ij} = \frac{1}{2}(\partial\tilde{u}_i/\partial x_j + \partial\tilde{u}_j/\partial x_i)$ is the filtered stain rate tensor, and $|\tilde{S}| = (2\tilde{S}_{ij}\tilde{S}_{ij})^{1/2}$. The isotropic part of the stress tensor on left-hand side, $\frac{1}{3}\tau_{kk}$, is neglected in this study based on the low Mach number flow assumption. C is the eddy-viscosity model constant.

In the dynamic Smagorinsky model (DSM), the model coefficient C is computed from the flowfield information extracted from the smallest resolved scales by applying a test-filter with width $\hat{\Delta}$ that is larger than the grid-filter width, Δ. The model coefficients are obtained by considering the difference between the subtest-scale and the SGS stresses [27–29]:

$$C\Delta^2 = \frac{\langle (\mathscr{L}_{ij} - \frac{1}{3}\mathscr{L}_{kk}\delta_{ij})\mathscr{M}_{ij}\rangle}{\langle \mathscr{M}_{ij}\mathscr{M}_{ij}\rangle}, \tag{26}$$

where

$$\mathscr{L}_{ij} = \widehat{\bar{\rho}\tilde{u}_i\tilde{u}_j} - \frac{1}{\hat{\bar{\rho}}}\widehat{\bar{\rho}\tilde{u}_i}\,\widehat{\bar{\rho}\tilde{u}_j}, \tag{27}$$

$$\mathscr{M}_{ij} = -2(\hat{\triangle}/\triangle)^2\hat{\bar{\rho}}|\hat{\tilde{S}}|(\hat{\tilde{S}}_{ij} - \frac{1}{3}\hat{\tilde{S}}_{kk}\delta_{ij}) + \overbrace{2\bar{\rho}|\tilde{S}|(\tilde{S}_{ij} - \frac{1}{3}\tilde{S}_{kk}\delta_{ij})}. \tag{28}$$

The angled brackets $\langle\,\rangle$ imply spatial averaging along homogeneous coordinate directions. The coefficient C was numerically restricted to always be non-negative, disallowing backscatter. Also, the SGS heat flux is specified in terms of a constant turbulent Prandtl number Pr_t as:

$$\mathscr{Q}_i = \frac{\mu_t}{Pr_t}\frac{\partial\tilde{T}}{\partial x_i} \tag{29}$$

consistent with the low Mach number and nearly uniform temperature distribution of the flows considered in this study.

3. Numerical methods

3.1. Spatial discretization

First derivatives at interior grid points away from the boundaries, f'_i, are determined using the following sixth-order compact finite-difference scheme of Lele [8]:

$$\frac{1}{3}f'_{i-1} + f'_i + \frac{1}{3}f'_{i+1} = \frac{7}{9\Delta\xi}(f_{i+1} - f_{i-1}) + \frac{1}{36\Delta\xi}(f_{i+2} - f_{i-2}) \tag{30}$$

shown here for grid point i along the ξ direction with $\Delta\xi$ as the uniform grid spacing. At the left and right boundary points, at $i = 1$ and $i = N$, respectively, the following third-order, one-sided compact schemes are used:

$$f'_1 + 2f'_2 = \frac{1}{2\Delta\xi}(-5f_1 + 4f_2 + f_3), \tag{31}$$

$$f'_N + 2f'_{N-1} = \frac{1}{2\Delta\xi}(5f_N - 4f_{N-1} - f_{N-2}). \tag{32}$$

For points adjacent to the boundaries, $i = 2$ and $i = N - 1$, the following fourth-order, central, compact schemes are used:

$$\frac{1}{4}f'_1 + f'_2 + \frac{1}{4}f'_3 = \frac{3}{4\Delta\xi}(f_3 - f_1), \tag{33}$$

$$\frac{1}{4}f'_{N-2} + f'_{N-1} + \frac{1}{4}f'_N = \frac{3}{4\Delta\xi}(f_N - f_{N-2}). \tag{34}$$

3.2. Temporal discretization

A three-stage, third-order, additive, semi-implicit Rosenbrock Runge–Kutta method (ASIRK-3C) is used for time advancement [10]. After spatial discretization, the governing equations can be expressed in semi-discrete form yielding the following system of first-order ODEs:

$$\frac{d\mathbf{u}}{dt} = \mathbf{f}(\mathbf{u}) + \mathbf{g}(\mathbf{u}), \tag{35}$$

where $\mathbf{u}$ is the vector of discretized flow field variables and t is time. In this study, $\mathbf{u}$ is the vector of conservative variables divided by J, the Jacobian of the coordinate transformation. The right-hand side of Eq. (35) is split into two parts $\mathbf{g}$ and $\mathbf{f}$, where $\mathbf{g}$ represents the spatial discretization of terms deemed stiff and $\mathbf{f}$ the spatial discretization of the remaining non-stiff terms in the equation. The ASIRK-3C scheme numerically integrates Eq. (35) by simultaneously treating $\mathbf{f}$ explicitly and $\mathbf{g}$ implicitly:

$$\mathbf{u}^{n+1} = \mathbf{u}^n + \sum_{j=1}^{3} \omega_j \mathbf{k}_j, \tag{36}$$

$$\left[\mathbf{I} - \Delta t a_i \mathbf{J}(\mathbf{u}^n + \sum_{j=1}^{i-1} c_{ij}\mathbf{k}_j)\right]\mathbf{k}_i = \Delta t\left\{\mathbf{f}\left(\mathbf{u}^n + \sum_{j=1}^{i-1} b_{ij}\mathbf{k}_j\right) + \mathbf{g}\left(\mathbf{u}^n + \sum_{j=1}^{i-1} c_{ij}\mathbf{k}_j\right)\right\} \quad (\text{for } i = 1,2,3), \tag{37}$$

where Δt is the time-step size, $\mathbf{I}$ is the identity matrix, $\mathbf{J} = \frac{\partial \mathbf{g}}{\partial \mathbf{u}}$ is the Jacobian matrix for the stiff term $\mathbf{g}$, and a_i, b_{ij}, c_{ij}, and ω_j are parameters determined by accuracy and stability considerations [10]. Note $\mathbf{J}$ is different from J which appeared in the context of the coordinate transformation. Implementation details relevant to $\mathbf{J}$ will be discussed in the following section. The parameters used here are:

$$\omega_1 = \frac{1}{8}, \quad \omega_2 = \frac{1}{8}, \quad \omega_3 = \frac{3}{4};$$
$$a_1 = 0.797097, \quad a_2 = 0.591381, \quad a_3 = 0.134705;$$
$$b_{21} = \frac{8}{7}, \quad b_{31} = \frac{71}{252}, \quad b_{32} = \frac{7}{36};$$
$$c_{21} = 1.05893, \quad c_{31} = \frac{1}{2}, \quad c_{32} = -0.375939;$$

where a_1, a_2, a_3, c_{21} and c_{32} are irrational numbers with six significant digits. The double precision values of these parameters are extracted from Zhong [10].

The explicit part of the algorithm establishes the stability limits for the method. For the third-order Runge–Kutta scheme, used together with the sixth-order compact scheme, the CFL condition for the pure advection case (on a periodic one-dimensional domain) is [8]:

$$\frac{c\Delta t}{\Delta x} \leqslant \frac{\sqrt{3}}{1.989}, \tag{38}$$

where c is advection speed and Δx is the step sizes in x. The stability criterion for the pure diffusion case (on a periodic one-dimensional domain) is given by [8]:

$$\frac{v\Delta t}{(\Delta x)^2} \leqslant \frac{2.5}{6.857}, \tag{39}$$

where v is a diffusion coefficient. Hence, the stable range of the CFL numbers is limited by the explicit parts of the scheme and diffusion terms. For the applications in this article, the range is limited between 5 and 7. The ASIRK-3C method is about twice as costly computationally as the fourth-order explicit Runge–Kutta scheme because of the need to invert a block pentadiagonal matrix system for every stage of time advancement. Overall, the ASIRK-3C scheme is between 2.5 and 3.5 times more efficient than the fourth-order explicit Runge–Kutta scheme because the present scheme is able to employ a 5–7 times larger time-step.

3.3. Implementation of ASIRK-3C with the compact scheme

In the present ASIRK-3C implementation, $\mathbf{g}$ is taken as the convective terms in the wall-normal direction and $\mathbf{f}$ represents all the other terms in the governing equations. The convective terms in the wall-normal direction can be written as $\frac{\partial \hat{\mathbf{G}}}{\partial \zeta}$, where the Jacobian matrix $\mathbf{J}$ becomes $\frac{\partial}{\partial \mathbf{u}}(\frac{\partial \hat{\mathbf{G}}}{\partial \zeta})$. Switching the order of differentiation, this term can be written as $\frac{\partial}{\partial \zeta}(\frac{\partial \hat{\mathbf{G}}}{\partial \mathbf{u}})$ and then the following equation is solved:

$$\left[\mathbf{I}-\alpha\frac{\partial}{\partial\zeta}\left(\frac{\partial\hat{\mathbf{G}}}{\partial\mathbf{u}}\right)\right]\mathbf{k}=\mathbf{RHS}, \tag{40}$$

where α, $\mathbf{k}$, and $\mathbf{RHS}$ represent the terms introduced in Eq. (37). Here, $\frac{\partial\hat{\mathbf{G}}}{\partial\mathbf{u}}$ is another Jacobian matrix, typically arising in Beam–Warming type implicit schemes [30]. To implement this equation with the compact schemes, an approach similar to that of Ekaterinaris' implicit algorithm is used [31]. For nodes away from the boundaries, the first-order derivatives are evaluated with the following compact scheme:

$$\frac{1}{3}f'_{k-1}+f'_k+\frac{1}{3}f'_{k+1}=\frac{7}{9\Delta\zeta}(f_{k+1}-f_{k-1})+\frac{1}{36\Delta\zeta}(f_{k+2}-f_{k-2}). \tag{41}$$

Applying a similar operation to Eq. (40),

$$\begin{aligned}&\frac{1}{3}\left[\mathbf{I}-\alpha\frac{\partial}{\partial\zeta}\left(\frac{\partial\hat{\mathbf{G}}}{\partial\mathbf{u}}\right)_{k-1}\right]\mathbf{k}_{k-1}+\left[\mathbf{I}-\alpha\frac{\partial}{\partial\zeta}\left(\frac{\partial\hat{\mathbf{G}}}{\partial\mathbf{u}}\right)_{k}\right]\mathbf{k}_k+\frac{1}{3}\left[\mathbf{I}-\alpha\frac{\partial}{\partial\zeta}\left(\frac{\partial\hat{\mathbf{G}}}{\partial\mathbf{u}}\right)_{k+1}\right]\mathbf{k}_{k+1}\\&\quad=\frac{1}{3}\mathbf{RHS}_{k-1}+\mathbf{RHS}_k+\frac{1}{3}\mathbf{RHS}_{k+1},\end{aligned} \tag{42}$$

where each subscript corresponds to the node location in the wall-normal direction (ζ). Using Eq. (41), Eq. (42) can be written in the following form:

$$\begin{aligned}&\left[\frac{\mathbf{I}}{3}+\frac{7}{9\Delta\zeta}\alpha\left(\frac{\partial\hat{\mathbf{G}}}{\partial\mathbf{u}}\right)_{k-1}\right]\mathbf{k}_{k-1}+[\mathbf{I}]\mathbf{k}_k+\left[\frac{\mathbf{I}}{3}-\frac{7}{9\Delta\zeta}\alpha\left(\frac{\partial\hat{\mathbf{G}}}{\partial\mathbf{u}}\right)_{k+1}\right]\mathbf{k}_{k+1}+\left[\frac{1}{36\Delta\zeta}\alpha\left(\frac{\partial\hat{\mathbf{G}}}{\partial\mathbf{u}}\right)_{k-2}\right]\mathbf{k}_{k-2}\\&\quad-\left[\frac{1}{36\Delta\zeta}\alpha\left(\frac{\partial\hat{\mathbf{G}}}{\partial\mathbf{u}}\right)_{k+2}\right]\mathbf{k}_{k+2}=\frac{1}{3}\mathbf{RHS}_{k-1}+\mathbf{RHS}_k+\frac{1}{3}\mathbf{RHS}_{k+1}.\end{aligned} \tag{43}$$

For nodes at or next to the boundaries, a similar approach can be taken with corresponding compact schemes. Finally, the block pentadiagonal matrix system can be solved.

3.4. Characteristic boundary conditions

Inlet and outlet boundary conditions were specified based on Kim and Lee's [32] generalized coordinate version of Poinsot and Lele's Navier–Stokes characteristic boundary conditions (NSCBC) [33]. The basic idea behind characteristic boundary conditions is to split the convective terms in the boundary-normal direction into several waves with different characteristic velocities and then express unknown incoming waves as a function of known outgoing waves. Brief implementation details for a Cartesian coordinate system will be followed by details related to extension for a body-fitted coordinate system.

Expressions for the convective terms in the boundary-normal direction with characteristic waves are shown here:

$$\begin{pmatrix}\frac{\partial(\rho u_1)}{\partial x_1}\\ \rho c^2\frac{\partial u_1}{\partial x_1}+u_1\frac{\partial p}{\partial x_1}\\ u_1\frac{\partial u_1}{\partial x_1}+\frac{1}{\rho}\frac{\partial p}{\partial x_1}\\ u_1\frac{\partial u_2}{\partial x_1}\\ u_1\frac{\partial u_3}{\partial x_1}\end{pmatrix}=\begin{pmatrix}L_1+\frac{\rho}{2c}(L_4+L_5)\\ \frac{\rho c}{2}(L_4+L_5)\\ \frac{1}{2}(L_4-L_5)\\ L_3\\ L_2\end{pmatrix}, \tag{44}$$

where x_1 is the boundary-normal coordinate, c is local speed of sound, and the L_i's are the amplitudes of characteristic waves each with characteristic velocity λ_i:

$$\lambda_1=\lambda_2=\lambda_3=u_1;\quad \lambda_4=u_1+c;\quad \lambda_5=u_1-c, \tag{45}$$

where λ_1 is the velocity for the entropy advection and λ_2 and λ_3 are the velocities of u_2 and u_3 advection, respectively, and λ_4 and λ_5 are the velocities of sound waves in positive and negative x_1 direction, respectively. The L_i's are given by:

$$\begin{aligned} L_1 &= \lambda_1\left(\frac{\partial \rho}{\partial x_1} - \frac{1}{c^2}\frac{\partial p}{\partial x_1}\right), \\ L_2 &= \lambda_2\left(\frac{\partial u_3}{\partial x_1}\right), \\ L_3 &= \lambda_3\left(\frac{\partial u_2}{\partial x_1}\right), \\ L_4 &= \lambda_4\left(\frac{1}{\rho c}\frac{\partial p}{\partial x_1} + \frac{\partial u_1}{\partial x_1}\right), \\ L_5 &= \lambda_5\left(\frac{1}{\rho c}\frac{\partial p}{\partial x_1} - \frac{\partial u_1}{\partial x_1}\right). \end{aligned} \tag{46}$$

At a subsonic outlet, four characteristic waves L_1, L_2, L_3, and L_4 are leaving the computational domain, whereas L_5 is entering the domain. The amplitude of the L_5 incoming acoustic waves is specified according to:

$$L_5 = K_{\text{out}}[(p - p_\infty)/\rho c], \tag{47}$$

where c is a speed of sound and K_{out} is a constant expressed as:

$$K_{\text{out}} = \sigma_{\text{out}}(1 - M_{\max}^2)(c/l). \tag{48}$$

where l is a characteristic length of the domain and $\sigma_{\text{out}} = 0$ is used here and so Eq. (47) is identical to Thompson's perfectly non-reflecting boundary condition [34]. At a subsonic inlet, four characteristic waves L_1, L_2, L_3, and L_4 are entering the computational domain, whereas L_5 is leaving the domain. Therefore, the amplitudes of the four waves L_1, L_2, L_3, and L_4 must be specified. For one of the cases considered here, namely the asymmetric planar diffuser flow case, results from a separate LES of turbulent channel flow are used to compute L_1, L_2, L_3, and L_4 using an approach similar to Poinsot and Lele [33]:

$$\begin{aligned} L_2 &= -\frac{\partial u_3}{\partial t}, \\ L_3 &= -\frac{\partial u_2}{\partial t}, \\ L_4 &= -2\frac{\partial u_1}{\partial t} + L_5, \\ L_1 &= \frac{\rho}{cT}\frac{\partial T}{\partial t} + \frac{\rho}{2c}(\gamma - 1)(L_4 + L_5), \end{aligned} \tag{49}$$

where L_5 is calculated from interior nodes because it is an outgoing wave.

The use of a curvilinear coordinate system to handle more complicated geometries is common in CFD. The approach of Kim and Lee [32] is used here to generalize the characteristic based boundary conditions described above. The generalized characteristics are calculated by the following matrix operation:

$$\mathbf{L} = \mathbf{P}^{-1} J\left\{\frac{\partial \hat{\mathbf{E}}}{\partial \xi} - \left[\mathbf{E}\frac{\partial}{\partial \xi}\left(\frac{\xi_x}{J}\right) + \mathbf{F}\frac{\partial}{\partial \xi}\left(\frac{\xi_y}{J}\right) + \mathbf{G}\frac{\partial}{\partial \xi}\left(\frac{\xi_z}{J}\right)\right]\right\}, \tag{50}$$

where $\mathbf{L}$ is now the vector of the characteristics amplitude in curvilinear coordinates, J is the Jacobian associated with the coordinate transformation, the terms in the square bracket are suggested by Kim and Lee [32] to preserve the conservative form of the governing equations in generalized coordinates and $\mathbf{P}^{-1}$ is a matrix of the form:

$$\mathbf{P}^{-1}=\begin{bmatrix} \mathbf{B}_o\cdot\mathbf{l}_x & (\gamma-1)\frac{u}{c^2}\tilde{\xi}_x & (\gamma-1)\frac{v}{c^2}\tilde{\xi}_x+\frac{\tilde{\xi}_z}{\rho} & (\gamma-1)\frac{w}{c^2}\tilde{\xi}_x-\frac{\tilde{\xi}_y}{\rho} & -\frac{\gamma-1}{c^2}\tilde{\xi}_x \\ \mathbf{B}_o\cdot\mathbf{l}_y & (\gamma-1)\frac{u}{c^2}\tilde{\xi}_y-\frac{\tilde{\xi}_z}{\rho} & (\gamma-1)\frac{v}{c^2}\tilde{\xi}_y & (\gamma-1)\frac{w}{c^2}\tilde{\xi}_y+\frac{\tilde{\xi}_x}{\rho} & -\frac{\gamma-1}{c^2}\tilde{\xi}_y \\ \mathbf{B}_o\cdot\mathbf{l}_z & (\gamma-1)\frac{u}{c^2}\tilde{\xi}_z+\frac{\tilde{\xi}_y}{\rho} & (\gamma-1)\frac{v}{c^2}\tilde{\xi}_z-\frac{\tilde{\xi}_x}{\rho} & (\gamma-1)\frac{w}{c^2}\tilde{\xi}_z & -\frac{\gamma-1}{c^2}\tilde{\xi}_y \\ \frac{c}{\rho}\left(\frac{\gamma-1}{2}M^2-\frac{\mathbf{v}\cdot\mathbf{l}_\xi}{c}\right) & \mathbf{C}_+\cdot\mathbf{l}_x & \mathbf{C}_+\cdot\mathbf{l}_y & \mathbf{C}_+\cdot\mathbf{l}_z & \frac{\gamma-1}{\rho c} \\ \frac{c}{\rho}\left(\frac{\gamma-1}{2}M^2+\frac{\mathbf{v}\cdot\mathbf{l}_\xi}{c}\right) & \mathbf{C}_-\cdot\mathbf{l}_x & \mathbf{C}_-\cdot\mathbf{l}_y & \mathbf{C}_-\cdot\mathbf{l}_z & \frac{\gamma-1}{\rho c} \end{bmatrix},$$

where the vectors used in this matrix are defined as follows:

$$\mathbf{B}_o=\left\{1-[(\gamma-1)/2]M^2\right\}l_\xi-(1/\rho)(\mathbf{v}\times\mathbf{l}_\xi),\quad \mathbf{C}_\pm=\pm(\mathbf{l}_\xi/\rho)-[(\gamma-1)/\rho c]\mathbf{v},$$
$$\mathbf{l}_\xi=(\tilde{\xi}_x,\tilde{\xi}_y,\tilde{\xi}_z)=\left(1\Big/\sqrt{\xi_x^2+\xi_y^2+\xi_z^2}\right)(\xi_x,\xi_y,\xi_z),\quad \mathbf{l}_x=(1,0,0),\quad \mathbf{l}_y=(0,1,0),\quad \mathbf{l}_z=(0,0,1),$$

where $\mathbf{v}$ is a velocity vector. Next $\mathbf{L}$ is converted to $\mathbf{L}^*$ following Eq. (49), where $\mathbf{L}^*$ is the newly updated amplitude of the characteristics from the boundary conditions. In generalized coordinates, the characteristics are expressed by the following equation:

$$L_i=\lambda_i\frac{\partial R_i}{\partial\xi}\quad (i=1,2,\ldots,5), \tag{51}$$

where characteristic velocities λ_i and $\delta\mathbf{R}$ are expressed as follows:

$$\delta\mathbf{R}=\left[\delta\rho-(1/c^2)\delta p,\ \delta\tilde{W},\ \delta\tilde{V},\ (1/\rho c)\delta p+\delta\tilde{U},\ (1/\rho c)\delta p-\delta\tilde{U}\right]^{\mathrm{T}},$$
$$\lambda=\left[U,\ U,\ U,\ U+c\sqrt{\xi_x^2+\xi_y^2+\xi_z^2},\ U-c\sqrt{\xi_x^2+\xi_y^2+\xi_z^2}\right]^{\mathrm{T}},$$
$$U=\xi_x u+\xi_y v+\xi_z w,$$
$$\delta\tilde{U}=\tilde{\xi}_x\delta u+\tilde{\xi}_y\delta v+\tilde{\xi}_z\delta w,\quad \delta\tilde{V}=-\tilde{\xi}_x\delta v+\tilde{\xi}_y\delta u,\quad \delta\tilde{W}=\tilde{\xi}_x\delta w-\tilde{\xi}_z\delta u.$$

Then the conservation-form, normal-flux derivative term can be corrected with the following relation:

$$\left(\frac{\partial\hat{\mathbf{E}}}{\partial\xi}\right)^*=\frac{1}{J}\mathbf{P}\mathbf{L}^*+\left[\mathbf{E}\frac{\partial}{\partial\xi}\left(\frac{\xi_x}{J}\right)+\mathbf{F}\frac{\partial}{\partial\xi}\left(\frac{\xi_y}{J}\right)+\mathbf{G}\frac{\partial}{\partial\xi}\left(\frac{\xi_z}{J}\right)\right], \tag{52}$$

where $\mathbf{P}$ is given by the following matrix:

$$\mathbf{P}=\begin{bmatrix} \tilde{\xi}_x & \tilde{\xi}_y & \tilde{\xi}_z & \frac{\rho}{2c} & \frac{\rho}{2c} \\ u\tilde{\xi}_x & u\tilde{\xi}_y-\rho\tilde{\xi}_z & u\tilde{\xi}_z+\rho\tilde{\xi}_y & \frac{\rho}{2c}(u+\tilde{\xi}_x c) & \frac{\rho}{2c}(u-\tilde{\xi}_x c) \\ v\tilde{\xi}_x+\rho\tilde{\xi}_z & v\tilde{\xi}_y & v\tilde{\xi}_z-\rho\tilde{\xi}_x & \frac{\rho}{2c}(v+\tilde{\xi}_y c) & \frac{\rho}{2c}(v-\tilde{\xi}_y c) \\ w\tilde{\xi}_x-\rho\tilde{\xi}_y & w\tilde{\xi}_y+\rho\tilde{\xi}_x & w\tilde{\xi}_z & \frac{\rho}{2c}(w+\tilde{\xi}_z c) & \frac{\rho}{2c}(w-\tilde{\xi}_z c) \\ \mathbf{b}\cdot\mathbf{l}_x & \mathbf{b}\cdot\mathbf{l}_y & \mathbf{b}\cdot\mathbf{l}_z & \frac{\rho}{2c}(H+c\mathbf{v}\cdot\mathbf{l}_\xi) & \frac{\rho}{2c}(H-c\mathbf{v}\cdot\mathbf{l}_\xi) \end{bmatrix},$$

where $\mathbf{b}$ and H are defined as follows:

$$\mathbf{b}=(|\mathbf{v}|^2/2)\mathbf{l}_\xi+\rho(\mathbf{v}\times\mathbf{l}_\xi),\quad H=|\mathbf{v}|^2/2+c^2/(\gamma-1).$$

Additional viscous conditions are needed when computing viscous flows for a well-defined problem [33]. The normal stresses at the inlet and the tangential stresses and the normal heat flux at the outlet were specified to have zero spatial gradient in the direction normal to the boundaries.

An approach similar to Giles [35] is used here for the wall boundaries. The approach is based on Fourier analysis, whose details are not included here. First, consider matrix $\mathbf{G}$ that transforms the conservative variables to the primitive variables as follows:

$$\begin{bmatrix} \delta\rho \\ \delta u \\ \delta v \\ \delta w \\ \delta p \end{bmatrix} = \mathbf{G} \begin{bmatrix} \delta q_1 \\ \delta q_2 \\ \delta q_3 \\ \delta q_4 \\ \delta q_5 \end{bmatrix}, \tag{53}$$

where **G** represents the following matrix:

$$\mathbf{G} = \begin{bmatrix} 1 & 0 & 0 & 0 & 0 \\ -u/\rho & 1/\rho & 0 & 0 & 0 \\ -v/\rho & 0 & 1/\rho & 0 & 0 \\ -1/\rho & 0 & 0 & 1/\rho & 0 \\ \frac{\gamma-1}{2}(u^2+v^2+w^2) & -(\gamma-1)u & -(\gamma-1)v & -(\gamma-1)w & \gamma-1 \end{bmatrix}.$$

Also, matrix **H** transforms the primitive variables to the characteristics variables and can be expressed as follows:

$$\begin{bmatrix} L_1 \\ L_2 \\ L_3 \\ L_4 \\ L_5 \end{bmatrix} = \mathbf{H} \begin{bmatrix} \delta\rho \\ \delta u \\ \delta v \\ \delta w \\ \delta p \end{bmatrix}, \tag{54}$$

where **H** is given by the following matrix:

$$\mathbf{H} = \begin{bmatrix} 1 & 0 & 0 & 0 & -1/c^2 \\ -\tilde{\zeta}_z & 0 & \tilde{\zeta}_x & 0 & 0 \\ \tilde{\zeta}_y & -\tilde{\zeta}_x & 0 & 0 & 0 \\ 0 & \tilde{\zeta}_x & \tilde{\zeta}_y & \tilde{\zeta}_z & 1/\rho c \\ 0 & -\tilde{\zeta}_x & -\tilde{\zeta}_y & -\tilde{\zeta}_z & 1/\rho c \end{bmatrix},$$

where ζ is the wall-normal direction. Following this, we can define a matrix **M** for wall boundary conditions. Since all velocity components are zero at the wall boundaries, the wave amplitudes L_1, L_2, and L_3 are all zero. For the upper boundaries (where $\zeta = \zeta_{\max}$), wave L_4 is outgoing and L_5 is incoming. With zero velocity conditions, local one-dimensional inviscid relations suggest:

$$L_5 = L_4. \tag{55}$$

Note that the wave direction is changed for the lower boundaries (where $\zeta = \zeta_1$). Consequently, this condition can be written in the following matrix form:

$$\begin{bmatrix} L_1^* \\ L_2^* \\ L_3^* \\ L_4^* \\ L_5^* \end{bmatrix} = \mathbf{M} \begin{bmatrix} L_1 \\ L_2 \\ L_3 \\ L_4 \\ L_5 \end{bmatrix}, \tag{56}$$

where **M** is given by:

$$\mathbf{M} = \begin{cases} \begin{bmatrix} 0 & 0 & 0 & 0 & 0 \\ 0 & 0 & 0 & 0 & 0 \\ 0 & 0 & 0 & 0 & 0 \\ 0 & 0 & 0 & 1 & 0 \\ 0 & 0 & 0 & 1 & 0 \end{bmatrix} & \text{for } \zeta = \zeta_{\max}, \\ \begin{bmatrix} 0 & 0 & 0 & 0 & 0 \\ 0 & 0 & 0 & 0 & 0 \\ 0 & 0 & 0 & 0 & 0 \\ 0 & 0 & 0 & 0 & 1 \\ 0 & 0 & 0 & 0 & 1 \end{bmatrix} & \text{for } \zeta = \zeta_1. \end{cases}$$

Upon updating the characteristic wave amplitudes, new boundary values can be computed using the inverse matrices, $\mathbf{G}^{-1}$ or $(\mathbf{HG})^{-1}$. In the original approach of Giles' these boundary-condition updates are processed explicitly at the end of each stage of time advancement [35]. However, here the wall boundary conditions need to be implemented implicitly because of the implicit treatment of the wall-normal convection terms. Thus, these whole matrix operations are performed as part of calculating the governing equations. An implicit wall boundary condition can be added in the governing equations at the wall boundary nodes by modifying Eq. (40):

$$\left[I - \alpha \mathbf{N} \frac{\partial}{\partial \zeta} \left(\frac{\partial \hat{\mathbf{G}}}{\partial \mathbf{u}} \right) \right] \mathbf{k} = \mathbf{N} \cdot \mathbf{RHS}, \tag{57}$$

where $\mathbf{N} = (\mathbf{HG})^{-1}\mathbf{MHG}$. However, it is undesirable to perform matrix multiplication with the term $\frac{\partial}{\partial \zeta}\left(\frac{\partial \hat{\mathbf{G}}}{\partial \mathbf{u}}\right)$ because this term should be modified using compact schemes. Therefore, the following equation is used for the wall-boundary nodes, replacing Eq. (40)

$$\left[\mathbf{N}^{-1} - \alpha \frac{\partial}{\partial \zeta} \left(\frac{\partial \hat{\mathbf{G}}}{\partial \mathbf{u}} \right) \right] \mathbf{k} = \mathbf{RHS}. \tag{58}$$

To obtain the inverse of matrix $\mathbf{N}$, very small values ($\epsilon \simeq 1.0\mathrm{e}^{-6}$) are placed at the diagonal elements of $\mathbf{M}$ matrix instead of zeroes:

$$\begin{bmatrix} L_1^* \\ L_2^* \\ L_3^* \\ L_4^* \\ L_5^* \end{bmatrix} = \mathbf{M}^* \begin{bmatrix} L_1 \\ L_2 \\ L_3 \\ L_4 \\ L_5 \end{bmatrix}, \tag{59}$$

where $\mathbf{M}^*$ is given by

$$\mathbf{M}^* = \begin{cases} \begin{bmatrix} \epsilon & 0 & 0 & 0 & 0 \\ 0 & \epsilon & 0 & 0 & 0 \\ 0 & 0 & \epsilon & 0 & 0 \\ 0 & 0 & 0 & 1 & 0 \\ 0 & 0 & 0 & 1 & \epsilon \end{bmatrix} & \text{for } \zeta = \zeta_{\max}, \\ \begin{bmatrix} \epsilon & 0 & 0 & 0 & 0 \\ 0 & \epsilon & 0 & 0 & 0 \\ 0 & 0 & \epsilon & 0 & 0 \\ 0 & 0 & 0 & \epsilon & 1 \\ 0 & 0 & 0 & 0 & 1 \end{bmatrix} & \text{for } \zeta = \zeta_1. \end{cases}$$

3.5. Exit zone for the outflow boundary

The exit-zone approach involves a smooth stretching of grid in the downstream region of the computational domain [36] and application of an artificial damping of the solution for nodes near the outlet to minimize acoustic reflections at the outlet boundary [37,38]. Consider coordinate s to be associated with a uniform grid with spacing Δs before stretching. The stretched grid coordinate x is given by following relation:

$$x = s + \frac{\Delta x_{\max}}{\sigma \Delta s} \ln[e^{\sigma(s-s_t)} + 1], \tag{60}$$

where

$$s_t = \frac{s_{\max}[1 + (\Delta x_{\max}/\Delta s)] - x_{\max}}{(\Delta x_{\max}/\Delta s)},$$
$$\sigma = \frac{\ln(\Delta x_{\max}/\delta \Delta s)}{s_t - x_p},$$
$$\delta = \frac{\Delta x_p}{\Delta s} - 1 = 0.00001$$

with $s_{\max}$ as the maximum value of coordinate s. Also, Δx_p and $\Delta x_{\max}$ are grid spacings at x_p (the point where stretching starts) and $x_{\max}$ (the point where stretching ends), respectively.

In the exit zone, an additional damping term is added to the right-hand side of the governing equations to drive the flow field toward the desired smooth solution as follows:

$$\frac{\partial \hat{\mathbf{Q}}}{\partial t} = \mathrm{RHS} - \sigma(x)(\hat{\mathbf{Q}} - \hat{\mathbf{Q}}_{\mathrm{target}}), \tag{61}$$

where

$$\sigma(x) = \sigma_{\max}\left(\frac{x - x_p}{x_{\max} - x_p}\right)^3,$$

$\sigma(x)$ controls the strength of the damping term and 1.0 is used for $\sigma_{\max}$. Also, x is the streamwise position, x_p and $x_{\max}$ are the streamwise coordinates of the end of physical region and the end of computational domain including exit zone, respectively, $\hat{\mathbf{Q}}$ is the vector of conservative variables, $\hat{\mathbf{Q}}_{\mathrm{target}}$ is the target solution in the exit zone and RHS is all terms in Eq. (1) except the time derivative of $\hat{\mathbf{Q}}$. In the diffuser simulation, the mean streamwise velocity profiles from the experiment [20] are specified as the target solution in the exit zone.

3.6. Filters for the LES

Padé-type filters, as derived by Lele [8], are used here for both grid- and test-filter operations associated with the dynamic Smagorinsky subgrid-scale turbulence model. The form of the filter is given in terms of

$$\beta \bar{f}_{i-2} + \alpha \bar{f}_{i-1} + \bar{f}_i + \alpha \bar{f}_{i+1} + \beta \bar{f}_{i+2} = a f_i + b(f_{i+1} + f_{i-1}) + c(f_{i+2} + f_{i-2}) + d(f_{i+3} + f_{i-3}), \tag{62}$$

where $\bar{f}_i$ represents the filtered value of f at the node i and the coefficients are:

$$a = \frac{2 + 3\alpha}{4}, \quad b = \frac{9 + 16\alpha + 10\beta}{32}, \quad c = \frac{\alpha + 4\beta}{8}, \quad d = \frac{6\beta - 1}{32}$$

and α and β will be determined by the filter size. The Fourier transform of the filter transfer function $\hat{G}(k)$ is given by:

$$\hat{G}(k) = \frac{a + 2b\cos(k) + 2c\cos(2k) + 2d\cos(3k)}{1 + \alpha\cos(k) + 2\beta\cos(2k)}. \tag{63}$$

Grid filters are defined by the coefficients $\alpha = 0.652247$ and $\beta = 0.170293$. These coefficients are derived by enforcing the following conditions on the filter transfer function, which adjust the location of cutoff of the filer:

$$\hat{G}(2.0) = 0.95;$$
$$\hat{G}(2.5) = 0.5.$$

For the nodes near boundaries, the fourth-order explicit filters introduced in Lele [8] are used. The test filters are defined by the coefficients $\alpha = 0.116053$ and $\beta = 0.279615$. These coefficients are derived by enforcing the following conditions on the filter transfer function:

$$\hat{G}\left(\frac{7}{6}\right) = 0.95;$$
$$\hat{G}\left(\frac{5}{3}\right) = 0.5.$$

The test filters are only applied in the streamwise and spanwise directions. The filter width ratio, defined as the ratio of the test-filter to grid-filter widths, is computed using the wave numbers at which the filter transfer function is equal to 0.5 [39]. Therefore, the filter width ratio is

$$\frac{\hat{\Delta}}{\Delta} = \left(\left[\frac{\hat{\Delta}}{\Delta}\right]_\xi \left[\frac{\hat{\Delta}}{\Delta}\right]_\eta \left[\frac{\hat{\Delta}}{\Delta}\right]_\zeta\right)^{\frac{1}{3}} = \left(\frac{2.5}{\frac{5}{3}}\right)^{\frac{2}{3}} = 1.5^{\frac{2}{3}} = 1.31037.$$

4. Results

4.1. One-dimensional wave propagation

Before applying the above model to study aeroacoustics of wall-bounded turbulent flows, it is important to assess the wave propagation capabilities of the semi-implicit method as implemented here. To test this, a code is written to solve the one-dimensional Euler equations for calorically perfect gas in a unit-length tube. Acoustic waves are generated at the left end of the tube by vibrating a *virtual* piston with amplitude $u_{\max}/c = 10^{-2}$ and dimensionless frequency of 5. At the right end of the tube we enforce a perfectly non-reflecting boundary condition (see Fig. 1). Hence, waves generated by the piston propagate with the mean flow, also about $u/c = 10^{-2}$, and simply leave the domain. The spatial discretization introduced in Section 3 is used. A plot showing the acoustic pressure waveform after a dimensionless time $1/c$ of 12.5 (sufficient for the wave to traverse the entire tube) is shown in Fig. 2 for several different time discretization schemes. The different schemes correspond to the classical fourth-order explicit Runge–Kutta (RK4) scheme and either *explicit* or *implicit* versions of the ASIRK-3C scheme. The *explicit* and *implicit* schemes with the CFL numbers of 0.5 and 2, respectively, give almost identical results with RK4. The *implicit* scheme with the CFL number of 5 is also in good agreement with RK4, showing only slight damping. The *implicit* scheme with the CFL number of 10 produces unacceptable levels of damping.

In the ASIRK-3C LES implementation, the streamwise and spanwise directions will be treated explicitly and the wall normal direction implicitly. Hence, it is assumed that acoustic waves are fully resolved (at least equivalent to what RK4 would produce). Only the wall-normal direction is affected by artificial damping associated with the implicit scheme. A refined mesh is used near the wall, and thus the artificial damping effects are assumed small in the target CFL number range of 5–7. Hence, acoustic waves are expected to be fully resolved in the simulations.

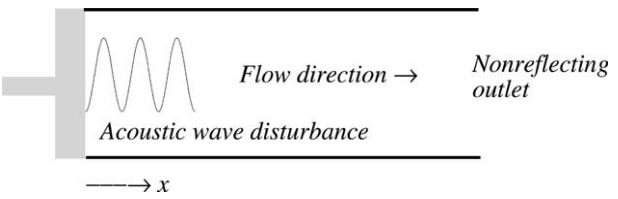

Fig. 1. Schematic of one-dimensional tube to test acoustic wave propagation capabilities of semi-implicit method.

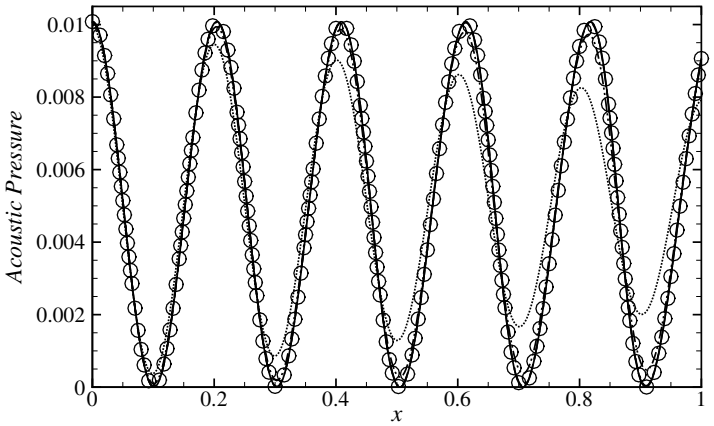

Fig. 2. Predicted acoustic pressure for the validation case of planar sound waves in a tube: fourth-order explicit RK/CFL=1.0 (○), third-order explicit RK/CFL = 0.5 (—), third-order implicit/CFL = 0.5 (---), third-order implicit/CFL = 2.0 (–·–·–), third-order implicit/CFL = 5.0(–··–), third-order implicit/CFL = 10.0 (·····).

4.2. Acoustic wave propagation in a channel

In order to test the performance of the boundary conditions introduced in Section 3 and the wave propagation in multi-dimensions using the semi-implicit scheme, another test simulation, similar to Mihăescu [40], was performed. Fig. 3 shows the geometry which consists of rectangular channel ($4 \times 1 \times 1$) featuring a smooth bump on the lower wall specified by:

$$z(x) = \begin{cases} 0 & \text{if } x \leqslant 1, \\ 0.1 \cdot \{1 - \cos[(x-1)\pi]\} & \text{if } 1 < x < 3, \\ 0 & \text{if } x \geqslant 3. \end{cases} \tag{64}$$

Non-reflecting boundary conditions, introduced in Section 3, are used at both ends of the x-coordinate and periodic conditions are applied for all variables in the y-direction. At the straight upper wall and curved lower wall, no-slip reflective boundary conditions are enforced using the formulation already introduced in Section 3. An initial density perturbation is imposed at the center of the domain by following function:

$$\rho'(r, t=0) = \begin{cases} \sin[0.5\pi(1 - \frac{r}{R})] & \text{if } r \leqslant R, \\ 0 & \text{if } r > R, \end{cases} \tag{65}$$

where R is the initial radius of the sphere of the disturbance taken here a 0.25. Also, r is the radial position ($\sqrt{x^2 + y^2 + z^2}$). This disturbance initiates wave propagation in the bumped channel. A Reynolds number of 20,000 based on the acoustic speed and channel height was used. A reference Mach number of 0.5 was used, which is low enough to maintain subsonic conditions everywhere. The maximum CFL number in the wall-normal

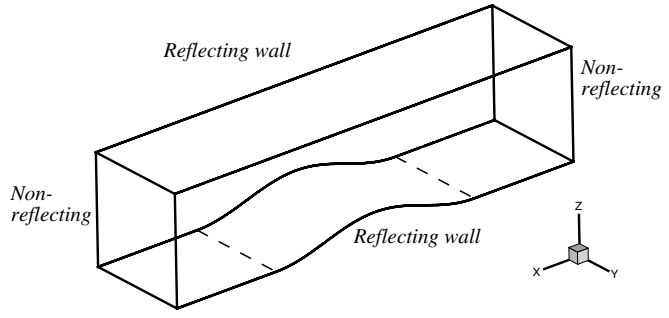

Fig. 3. The geometry of a channel with a bumped lower wall.

direction is 3.897. Fig. 4 shows a time sequence of the pressure distribution at the mid-plane in y-coordinate and highlights the wave propagation in the bumped channel. It is clear that the reflecting boundary conditions at both walls work properly. Also, it can be confirmed that the waves simply leave the domain through the non-reflecting boundary conditions at the side of the channel.

4.3. Turbulent channel flow

LES predictions were obtained for fully developed turbulent channel flow with a Reynolds numbers based on bulk velocity, U_b, and channel half-height, δ, of 2800, and a Mach number based on bulk velocity of 0.1. The bulk velocity is defined as:

$$U_b = \frac{1}{2\delta}\int_{-\delta}^{\delta} \tilde{u}\,dy. \tag{66}$$

Here, x, y, and z are taken as the streamwise, spanwise and wall-normal directions, respectively. The same non-dimensional computational domain size as the $Re_\tau = 180$ DNS case of Moser et al. [41] is used. A con-

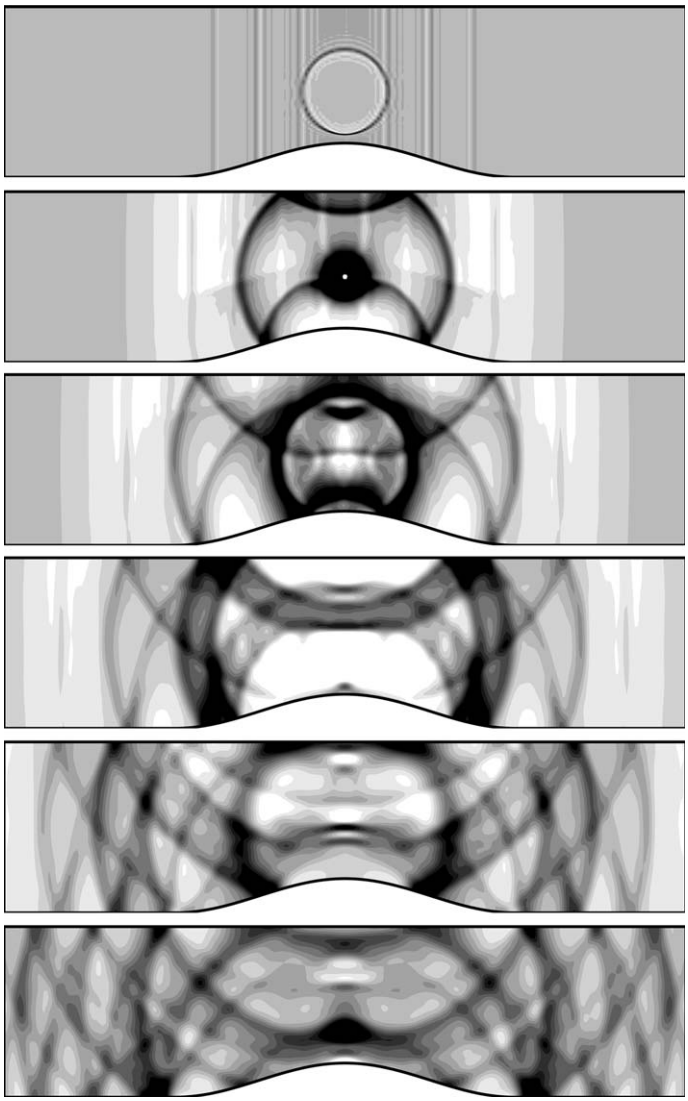

Fig. 4. A time sequence of the wave propagation in a channel with a bumped lower wall.

stant mesh spacing is used in the x and y directions. A non-uniform mesh spacing is used in the z direction based on the following transformation [13]:

$$z_k = \frac{1}{a}\tanh[\xi_k \tanh^{-1}(a)] \tag{67}$$

with

$$\xi_k = -1 + 2(k-1)/(N_3 - 1) \quad (k = 1, 2, \ldots, N_3),$$

where N_3 is the total number of grid points in the z-direction, and a is an adjustable transformation parameter ($0 < a < 1$); a large value of a distributes more points near the walls. In this study, $a \approx 0.98$ is used. Three cases are simulated and their mesh characteristics are listed in Table 1. Parameter Re_τ is a Reynolds number based on the friction velocity. The results of these cases are compared with the DNS results [41] for validation. Periodic boundary conditions are enforced for all variables in the streamwise and spanwise directions. At the channel walls, the wall boundaries introduced in Section 3 are used. An artificial forcing mechanism is needed to mimic an imposed streamwise pressure gradient and to maintain a fixed mass flow rate [18]. In this study, we employ the artificial forcing algorithm suggested by Rizzetta et al. [18] for the source term appearing in Eq. (1). The vector source term $\mathbf{S}$ is defined by:

$$\mathbf{S} = (1/J)[0, s_1, s_2, s_3, s_i\tilde{u}_i]^{\mathrm{T}}. \tag{68}$$

Considering the steady two-dimensional limiting form of the momentum equation in the streamwise direction and integrating over the channel height, we obtain:

$$s_1 = -\left[Re \int \left(\frac{1}{J}\right) \mathrm{d}\zeta\right]^{-1} \left\{ \left[\left(\frac{\tilde{\mu}\zeta_z^2}{J}\right)\frac{\partial \tilde{u}}{\partial \zeta}\right]_{\zeta=\zeta_{\max}} - \left[\left(\frac{\tilde{\mu}\zeta_z^2}{J}\right)\frac{\partial \tilde{u}}{\partial \zeta}\right]_{\zeta=\zeta_1} \right\}, \tag{69}$$

$$s_2 = s_3 = 0, \tag{70}$$

where the terms in square brackets imply averaging over the lower or upper channel walls. A Poiseuille parabolic streamwise velocity profile is used to initialize the streamwise velocity and random velocity fluctuations were superimposed on all three velocity components [17]. The flow field begins to reach a turbulent state after about 40,000 steps and 120,000 steps were sufficient for the flow to develop into a fully turbulent state. The maximum CFL number in the wall-normal direction in all simulations is about 6 and flow statistics were collected for 120,000 steps for each case. The code employs a streamwise domain decomposition and the MPI inter-processor communication libraries to facilitate parallel computation on an IBM-SP computer. For grid F case, a total of about 270 CPU hours on 16 processors were needed with communication time about 30% of total computation time.

Predicted mean flow variables for all cases presented in this paper, along with the DNS results of Kim et al. [42], are shown in Table 1. U_c/U_b, C_f and U_c^+ are the ratio of centerline velocity to bulk velocity, skin friction coefficients based on the bulk velocity and centerline velocity, normalized by the friction velocity u_τ, respectively.

The mean centerline velocities for all cases are in very good agreement with the value 1.158 obtained from the correlation of Dean [43]:

$$U_c/U_b = 1.28(2Re_b)^{-0.0116}. \tag{71}$$

The skin friction coefficient, C_f, computed for grid F, is within 10% of the value 8.438×10^{-3} given by Dean [43]:

Table 1
Simulation parameters for turbulent channel flow

Grid	$L_1 \times L_2 \times L_3$	$N_1 \times N_2 \times N_3$	Re_τ	Re_b	U_c/U_b	C_f	U_c^+
C	$4\pi \times 4/3\pi \times 2$	$48 \times 48 \times 49$	165.42	2800	1.14	6.80×10^{-3}	19.49
M	$4\pi \times 4/3\pi \times 2$	$64 \times 64 \times 65$	171.73	2800	1.14	7.37×10^{-3}	18.78
F	$4\pi \times 4/3\pi \times 2$	$80 \times 80 \times 81$	174.13	2800	1.14	7.60×10^{-3}	18.56
DNS [41]	$4\pi \times 4/3\pi \times 2$	$128 \times 128 \times 129$	178.13	2800	–	–	18.30
DNS [42]	$4\pi \times 2\pi \times 2$	$192 \times 160 \times 129$	180.00	2800	1.16	8.18×10^{-3}	18.20

$$C_f = 0.073(2Re_b)^{-0.25}. \quad (72)$$

It should be noted that Dean's correlation is for the Reynolds number range: $6.0 \times 10^3 < Re < 6.0 \times 10^5$ which is higher than the present case. The LES results on grid *F* are within 7% of the DNS value and the mean centerline velocities are also in good agreement with the DNS values.

In the simulations, all mean values and root mean square (RMS) values are averaged over $x-y$ planes with only periodic boundaries. Fig. 5 shows the time-averaged streamwise velocity profile, normalized by the friction velocity, on a logarithmic axis. For grid M and F cases, the graphs show good agreement between the present LES results and the previous DNS results [41], especially in the viscous sublayer ($z^+ \leqslant 5$) and logarithmic region. There is a slight overprediction of about 2% near the centerline that is most likely due to enhanced dissipation leading to an underprediction of the skin friction velocity u_τ due to the combined influences of the subgrid-scale model, the mesh resolution, and the other numerical methods. The LES studies of Lenormand et al. [17] and Okong and Knight [16] have observed similar overshoots when using the Smagorinsky SGS model. Visbal and Rizzetta [44] also found that using both the non-dynamic or dynamic version of the Smagorinsky model produced more dissipative results than results obtained using a high-order compact filtering procedure without any SGS model [18]. Our LES predictions are in as good, if not better, agreement with the DNS results than these other LES studies.

The RMS values for all three velocity components, normalized by friction velocity, are shown in Fig. 6, together with the DNS results [41]. The profile of streamwise velocity fluctuations from the grid F case is in very good agreement with the DNS results. The location and value of the peak are also well predicted (within 0.05% relative error and the location is $z^+ \simeq 15$). The spanwise and wall-normal velocity fluctuations are also in good agreement with the DNS data. The effect of grid resolution on streamwise velocity fluctuations is shown in this figure. A similar trend is observed for the other two velocity components (not shown). The LES result approaches the DNS result as the mesh is refined. Good agreement is observed between grid M and F cases.

LES predictions of the Reynolds shear stress profile, normalized by u_τ^2 and plotted in Fig. 7, show a slight underprediction near $z \simeq 0.2$. A consistent trend is observed as the grid is refined. It should be noted that for all profiles, except the streamwise velocity fluctuation, the largest discrepancy occurs in the region near $z = 0.15$–0.25 or $z^+ = 25$–45. This is where the maximum streamwise velocity gradient occurs and where the SGS stress terms are largest.

Examination of the instantaneous flow structures within the channel reveals characteristic features of fully developed turbulent channel flow such as regions of large streamwise vorticity concentrated near the walls (see Fig. 8) and streamwise velocity streaks (see Fig. 9). To further identify large-scale flow structures, an iso-surface of the second invariant of the filtered velocity gradient tensor $\nabla\tilde{\mathbf{v}}$ superposed on top of contours of streamwise velocity in a near-wall and transverse plane is shown in Fig. 10. The second invariant Q is:

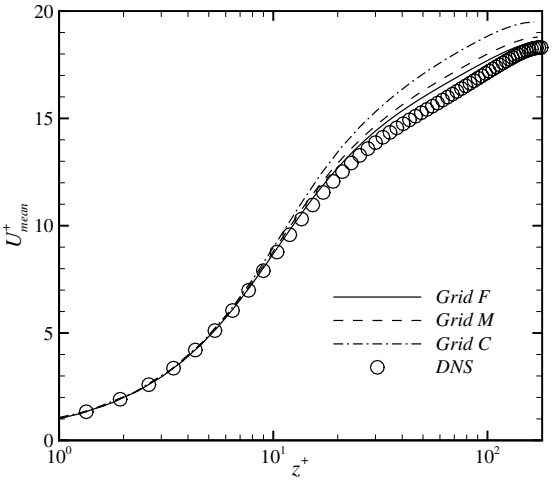

Fig. 5. Mean streamwise velocity profiles for the channel flow case; logarithmic plot showing comparison to previous DNS data for different grids.

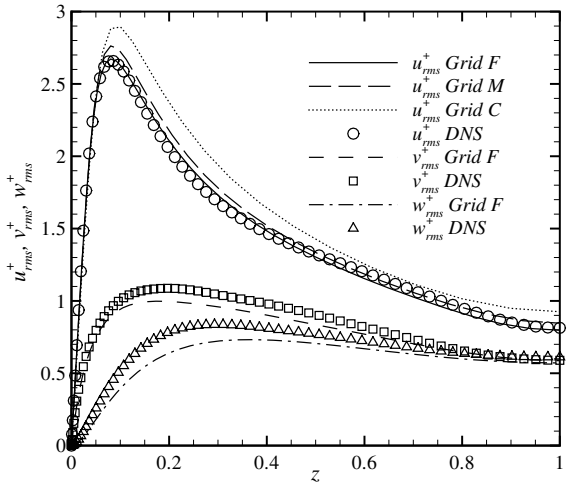

Fig. 6. Streamwise, transverse, and spanwise velocity fluctuations for the channel flow case using grid F; comparison to previous DNS data; effect of grid refinement of streamwise velocity fluctuation.

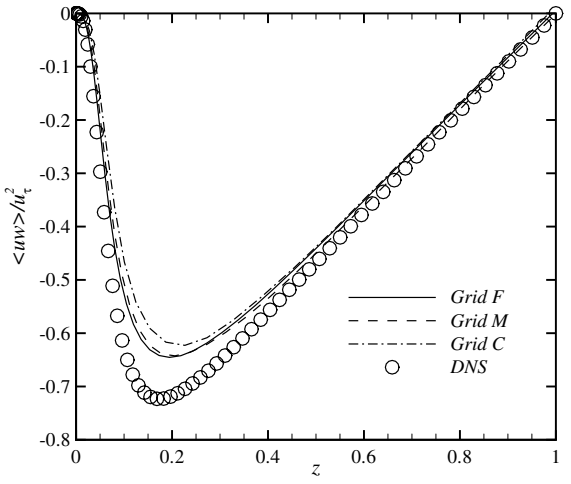

Fig. 7. Reynolds stress profile for the channel flow case; comparison to previous DNS data for different grids.

$$Q = 1/2(\Omega_{ij}\Omega_{ij} - S_{ij}S_{ij}), \tag{73}$$

where $\Omega_{ij} = (\tilde{u}_{i,j} - \tilde{u}_{j,i})/2$ and $S_{ij} = (\tilde{u}_{i,j} + \tilde{u}_{j,i})/2$ are the antisymmetric and the symmetric components of $\nabla\tilde{\mathbf{v}}$, respectively. The dominant coherent structures appear to be elongated, quasi-streamwise vortices of about 200 wall units in length. These structures are inclined about 10° in the vertical plane and tilted about ±5° in the horizontal plane. These observations are consistent with those of Jeong et al. [45].

4.4. Turbulent diffuser flow

4.4.1. Flow field

The second turbulent flow validation test case compares LES predictions of a separated turbulent flow in the planar asymmetric diffuser with experimental data obtained by Buice and Eaton [20]. The geometry and computational grid used for this study are presented in Figs. 11 and 12, respectively.

A structured grid consisting of $320 \times 64 \times 65$ points in the streamwise, spanwise, and wall-normal directions, respectively, is used. A similar mesh clustering method used in the channel flow simulation is used to resolve the near-wall region in the diffuser. Uniform grid spacing in the spanwise direction was used. The mesh

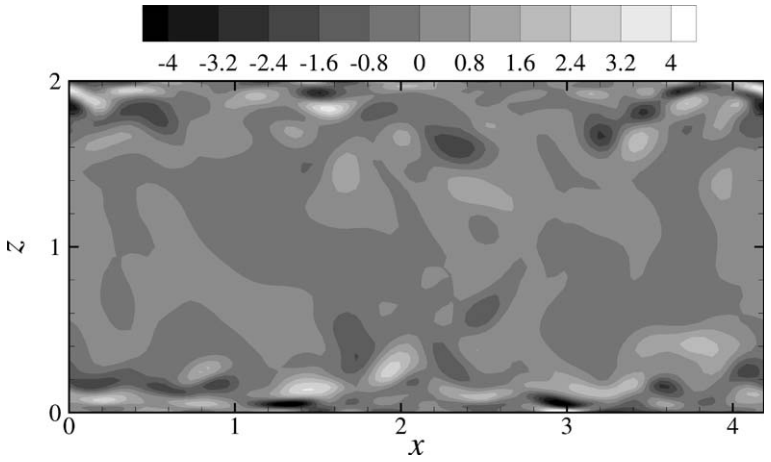

Fig. 8. Contour plot of the instantaneous streamwise vorticity in the (y,z)-plane for the channel flow case; grid F.

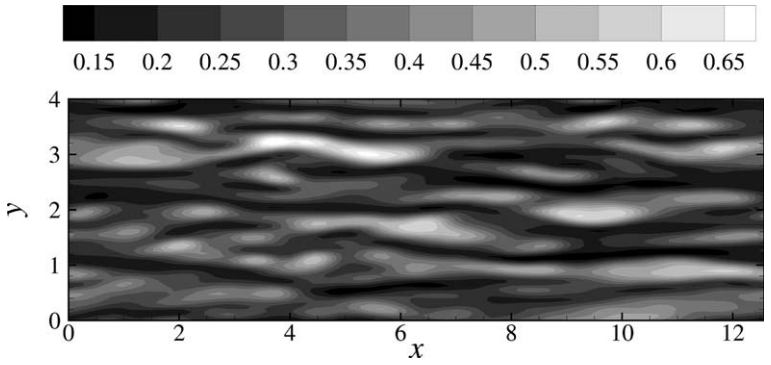

Fig. 9. Contour plot of the instantaneous streamwise velocity in the (x,y)-plane at $z^+ = 4.60$ for the channel flow case; grid F.

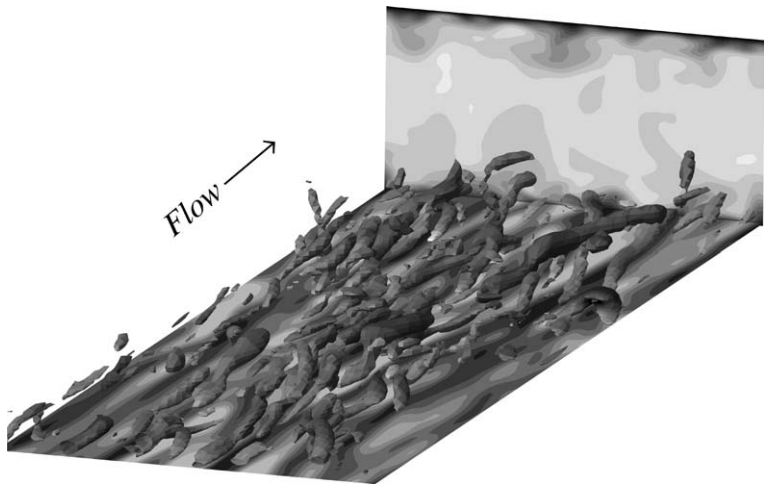

Fig. 10. Iso-surfaces of the second invariant of velocity deformation tensor superimposed on streamwise velocity contour near the wall at $z^+ = 4.60$ and for a transverse plane for the channel flow case; grid F.

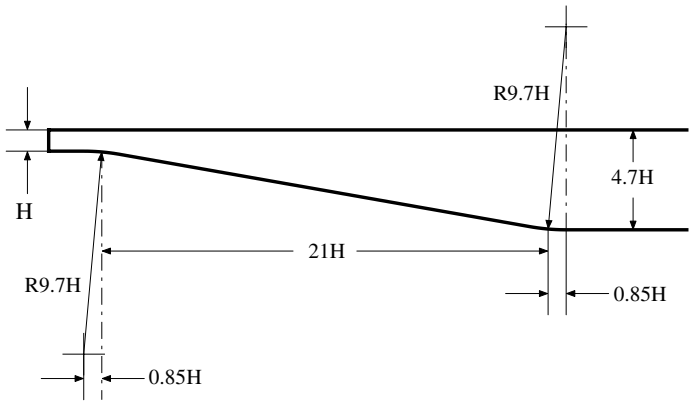

Fig. 11. Drawing of asymmetric diffuser geometry [20].

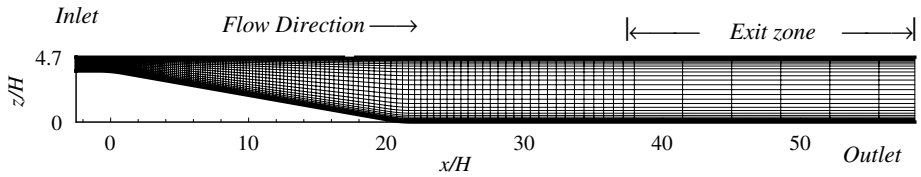

Fig. 12. Computational grid (every 2nd node is shown).

in the streamwise direction was stretched to resolve the throat region. Periodic boundary conditions were used for all variables in the spanwise direction. At the wall, the wall boundary conditions introduced in Section 3 were used. The inlet conditions were specified as a fully developed channel flow at Mach number 0.1 and $Re = 9000$ based on the bulk velocity and the inlet channel half-height. The inlet plane is located at $x/H = -2.5$ where the effect of the expansion part on the upstream is negligible [21]. Turbulent inlet conditions were determined by employing an auxiliary turbulent channel flow simulation ($L_1 \times L_2 \times L_3 = \pi H \times 2H \times H$, $N_1 \times N_2 \times N_3 = 64 \times 64 \times 65$) similar to that presented in the previous section. The channel flow simulation provided an unsteady Dirichlet boundary condition through the characteristic boundary condition formulation presented in Section 3. At the outflow of the domain, the characteristic outlet boundary condition and exit zone, described in Section 3, was used. The exit zone was located from $x/H = 27.5$ (same to the location of the outlet in Kaltenbach et al. [21]) to $x/H = 61$ and employs 14 points out of the 320 grid points used in the streamwise direction. The width of the diffuser was $2H$. The maximum CFL number in wall-normal direction was again 6. Initially 120,000 steps were used to develop flow field and flow statistics were collected after that for additional 120,000 steps. A total of about 580 CPU hours were needed on an IBM-SP machine using 32 processors in parallel to complete the simulation.

LES predictions of the mean streamwise velocity, normalized by the bulk velocity, are plotted against the experimental data in Fig. 13. Agreement between predictions and experimental data is good within the diffuser region, but discrepancies are noted in the downstream half of the diffuser region possibly due to the insufficient grid resolution for this region. Wall normal velocity fluctuations are also in reasonable agreement with the experiment as shown in Fig. 14. Several extended reverse flow regions along the lower deflected wall, with weaker reversed flow noted on the upper flat wall, can be observed in a contour plot of instantaneous streamwise velocity shown in Fig. 15.

4.4.2. Acoustic field

Lighthill transformed the continuity and Navier–Stokes equations to form an exact, inhomogeneous wave equation whose source term is called the Lighthill source tensor defined as [46]:

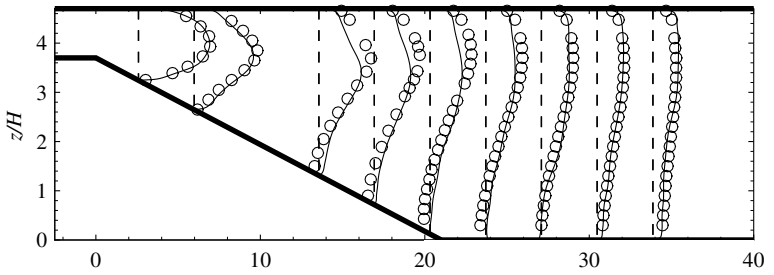

Fig. 13. Mean streamwise velocity $x/H + 5 \times U/U_b$: Present (—), Buice (○).

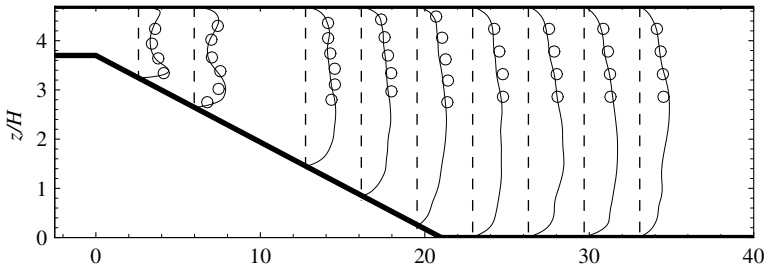

Fig. 14. Wall normal velocity fluctuation $x/H + 25 \times w_{rms}/U_b$: Present (—), Buice (○).

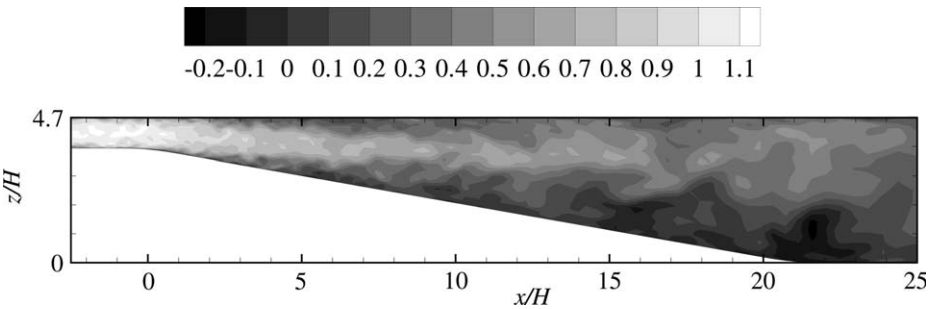

Fig. 15. Contour of the instantaneous streamwise velocity in (x, z)-plane for the diffuser flow.

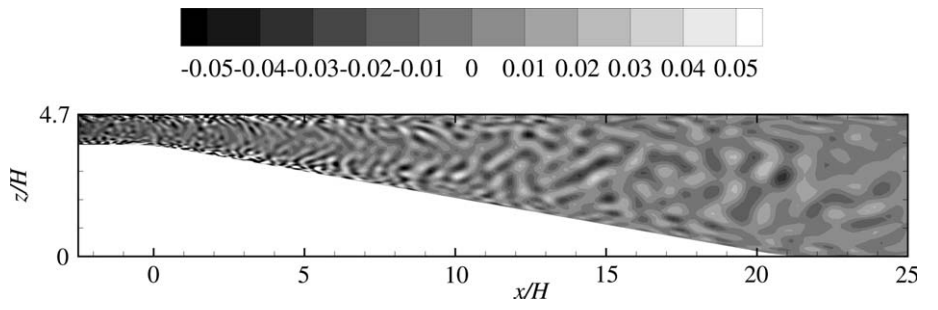

Fig. 16. Contour of the instantaneous dilatation in (x, z)-plane for the diffuser flow.

$$T_{ij} = \rho u_i u_j + \delta_{ij}(p' - c_\infty^2 \rho') - \sigma_{ij}. \tag{74}$$

In this equation σ_{ij} is the viscous stress tensor. Also $p' = p - p_\infty$ and $\rho' = \rho - \rho_\infty$ with p_∞, ρ_∞ and c_∞ representing the far-field pressure, density and sound speed, respectively. The Ffowcs Williams–Hawking equation may be used to account for the presence of solid surfaces [47]. In an uniform infinite duct, the sound sources are dominated by dipole sources due to pressure fluctuations along the walls [48]. A contour plot of the instantaneous dilatation $\Theta = \partial\tilde{u}_i/\partial x_i$ for the diffuser flow is shown in Fig. 16. Instantaneously, small-scales dominate the source near the walls of inlet and within the diffuser ahead of the separation zone. Their impact on the acoustic far-field will be the subject of future work.

5. Conclusion

As a first step towards conducting efficient computational aeroacoustics of wall-bounded turbulent flows, an LES code has been developed and tested for both attached and separated wall-bounded turbulent flows. The code combines the low-dissipation and dispersion through the use of a sixth-order accurate, compact finite-difference scheme for spatial derivatives. The third-order additive semi-implicit Runge–Kutta method is used for time advancement, treating wall-normal convective terms implicitly and allowing CFL numbers 5–7 times larger than a similar explicit code, while minimizing the amount of numerical damping present in the solution. Taking into account the additional computational overhead of the semi-implicit scheme, the algorithm is approximately 3 times faster than a similar accuracy explicit code. Characteristic-based non-reflecting boundary conditions applied in a generalized curvilinear coordinate system were used with special modifications at the wall to address the implicit time advancement. LES predictions were in reasonable agreement with previous numerical and experimental data for fully developed turbulent channel flow and turbulent separated flow in a planar asymmetric diffuser. Future work will focus on applications of this method for CAA studies of wall-bounded turbulent flows.

Acknowledgments

This work is supported by Research Grant No. R01-DC03577 from the National Institute on Deafness and other Communication Disorders, National Institutes of Health. The simulations presented in this paper were performed using the IBM-SP at Indiana University, and the IBM-SP at Purdue University. Dr. Wei Zhao wrote the original version of the code used here and discussions with him regarding implementation of the semi-implicit method are gratefully acknowledged.

References

[1] T. Colonius, S.K. Lele, Computational aeroacoustics: progress on nonlinear problems of sound generation, Prog. Aerosp. Sci. 40 (2004) 345–416.
[2] C. Wall, C.D. Pierce, P. Moin, A semi-implicit method for resolution of acoustic waves in low Mach number flows, J. Comput. Phys. 181 (2002) 545–563.
[3] J. Sesterhenn, B. Müller, H. Thomann, Flux-vector splitting for compressible low Mach number flow, Comput. Fluids 22 (1993) 441–451.
[4] G. Patnaik, R.H. Guirguis, J.P. Boris, E.S. Oran, A barely implicit correction for flux-corrected transport, J. Comput. Phys. 71 (1987) 1–20.
[5] L.D. Dailey, R.H. Pletcher, Evaluation of multigrid acceleration for preconditioned time-accurate Navier–Stokes algorithms, Comput. Fluids 25 (1996) 791–811.
[6] J. Weiss, J.P. Maruszewski, W. Smith, Implicit solution of preconditioned Navier–Stokes equations using algebraic multigrid, AIAA J. 37 (1999) 29–36.
[7] C.M. Shieh, P.J. Morris, High-order accurate dual time-stepping algorithm for viscous aeroacoustics simulations, AIAA Paper 98-2361, 1998.
[8] S.K. Lele, Compact finite difference schemes with spectral-like resolution, J. Comput. Phys. 103 (1992) 16–42.
[9] J.B. Freund, Noise sources in a low-Reynolds-number turbulent jet at Mach 0.9, J. Fluid Mech. 438 (2001) 277–305.
[10] X. Zhong, Additive semi-implicit Runge–Kutta methods for computing high-speed nonequilibrium reactive flows, J. Comput. Phys. 128 (1996) 19–31.
[11] X. Zhong, High-order finite-difference schemes for numerical simulation of hypersonic boundary-layer transition, J. Comput. Phys. 144 (1998) 662–709.

[12] H. Dong, X. Zhong, High-order semi-implicit schemes for unsteady compressible flow simulations, AIAA J. 40 (2002) 869–878.
[13] P. Moin, J. Kim, Numerical investigation of turbulent channel flow, J. Fluid Mech. 118 (1982) 341–377.
[14] U. Piomelli, High Reynolds number calculations using the dynamic subgrid-scale stress model, Phys. Fluids A 5 (1993) 1484–1490.
[15] S. Stolz, N.A. Adams, L. Kleiser, An approximate deconvolution model for large-eddy simulation with application to incompressible wall-bounded flows, Phys. Fluids 13 (2001) 997–1015.
[16] N. Okong, D.D. Knight, Compressible large eddy simulation using unstructured grids: channel and boundary layer flows, AIAA Paper 98-3315, 1998.
[17] E. Lenormand, P. Sagaut, L. Ta Phuoc, Large eddy simulation of subsonic and supersonic channel flow at moderate Reynolds number, Int. J. Numer. Meth. Fluids 32 (2000) 369–406.
[18] D.P. Rizzetta, M.R. Visbal, G.A. Blaisdell, A time-implicit high-order compact differencing and filtering scheme for large-eddy simulation, Int. J. Numer. Meth. Fluids 42 (2003) 665–693.
[19] S. Obi, K. Aoki, S. Masuda, Experimental and computational study of turbulent separating flow in an asymmetric plane diffuser, in: Ninth Symposium on Turbulent Shear Flows, Kyoto, Japan, 1993. p. 305. Accessible via: <ftp://ftp.mh.sd.keio.ac.jp/pub/Forced/Wall/fw_bl014.csv>.
[20] C.U. Buice, J.K. Eaton, Experimental investigation of flow through an asymmetric plane diffuser, J. Fluids Eng. 122 (2000) 433–435. Accessible via: <http://tmdb.ws.tn.tudelft.nl/workshop8/case8_2/case8_2.html>.
[21] H.-J. Kaltenbach, M. Fatica, R. Mittal, T.S. Lund, P. Moin, Study of flow in a planar asymmetric diffuser using large-eddy simulation, J. Fluid Mech. 390 (1999) 151–185.
[22] P.A. Durbin, Separated flow computation with the k–ϵ–v^2 model, AIAA J. 33 (1995) 659–664.
[23] G. Iaccarino, Predictions of a turbulent separated flow using commercial CFD codes, J. Fluids Eng. 123 (2001) 819–828.
[24] D.D. Apsley, M.A. Leschziner, Advanced turbulence modelling of separated flow in a diffuser, Flow Turbul. Combust. 63 (1999) 81–112.
[25] J. Gullman-Strand, O. Törnblom, B. Lindgren, G. Amberg, A.V. Johansson, Numerical and experimental study of separated flow in a plane asymmetric diffuser, Int. J. Heat Fluid Flow 25 (2004) 451–460.
[26] G. Erlebacher, M.Y. Hussaini, C.G. Speziale, T.A. Zang, Toward the large-eddy simulation of compressible turbulent flows, J. Fluid Mech. 238 (1992) 155–185.
[27] M. Germano, U. Piomelli, P. Moin, W.H. Cabot, A dynamic subgrid-scale eddy viscosity model, Phys. Fluids A 3 (1991) 1760–1765.
[28] P. Moin, P. Squires, W.H. Cabot, S. Lee, A dynamic subgrid-scale model for compressible turbulence and scalar transport, Phys. Fluids A 3 (1991) 2746–2757.
[29] D.K. Lilly, A proposed modification of the Germano subgrid-scale closure model, Phys. Fluids A 4 (1992) 633–635.
[30] J.V. Tannehill, D.A. Anderson, R.H. Pletcher, Computational Fluid Mechanics and Heat Transfer, second ed., Taylor & Francis, Levitton, PA, 1997.
[31] J.A. Ekaterinaris, Implicit, high-resolution, compact schemes for gas dynamics and aeroacoustics, J. Comput. Phys. 156 (1999) 279–299.
[32] J.W. Kim, D.J. Lee, Generalized characteristic boundary conditions for computational aeroacoustics, AIAA J. 38 (2000) 2040–2049.
[33] T.J. Poinsot, S.K. Lele, Boundary conditions for direct simulations of compressible viscous flows, J. Comput. Phys. 101 (1992) 104–129.
[34] K.W. Thompson, Time dependent boundary conditions for hyperbolic systems, J. Comput. Phys. 68 (1987) 1–24.
[35] M.B. Giles, Nonreflecting boundary conditions for Euler equation calculations, AIAA J. 28 (1990) 2050–2058.
[36] T. Colonius, S.K. Lele, P. Moin, Boundary conditions for direct computation of aerodynamic sound generation, AIAA J. 31 (1993) 1574–1582.
[37] J.B. Freund, Proposed inflow/outflow boundary condition for direct computation of aerodynamic sound, AIAA J. 35 (1997) 740–742.
[38] A. Uzun, 3-D large eddy simulation for jet aeroacoustics, Ph.D. Thesis, School of Aeronautics and Astronautics, Purdue University, West Lafayette, IN, December, 2003.
[39] W. Zhao, A numerical investigation of sound radiated from subsonic jets with application to human phonation, Ph.D. Thesis, School of Mechanical Engineering, Purdue University, West Lafayette, IN, August, 2000.
[40] M. Mihăescu, R.-Z. Szasz, L. Fuchs, E. Gutmark, Numerical investigation of the acoustics of a coaxial nozzle, AIAA Paper 2005-420, 2005.
[41] R.D. Moser, J. Kim, N.N. Mansour, Direct numerical simulation of turbulent channel flow up to $Re_\tau = 590$, Phys. Fluids 11 (1999) 943–945. Accessible via: <http://www.tam.uiuc.edu/Faculty/Moser/channel> .
[42] J. Kim, P. Moin, R.D. Moser, Turbulence statistics in fully developed channel flow at low Reynolds number, J. Fluid Mech. 177 (1987) 133–166.
[43] R.B. Dean, Reynolds number dependence of skin friction and other bulk flow variables in two-dimensional rectangular duct flow, J. Fluids Eng. 100 (1978) 215–223.
[44] M.R. Visbal, D.P. Rizzetta, Large-eddy simulation on curvilinear grids using compact differencing and filtering schemes, J. Fluids Eng. 124 (2002) 836–847.
[45] J. Jeong, F. Hussain, W. Schoppa, J. Kim, Coherent structures near the wall in a turbulent channel flow, J. Fluid Mech. 332 (1997) 185–214.
[46] M.J. Lighthill, On sound generated aerodynamically, I. General theory, Proc. R. Soc. Lond., Ser. A 211 (1952) 546–587.
[47] J.E. Ffowcs Williams, D.L. Hawkings, Sound generation by turbulence and surfaces in arbitrary motion, Philos. Trans. R. Soc. Lond., Ser. A 264 (1969) 321–342.
[48] W. Zhao, S.H. Frankel, L. Mongeau, Numerical simulation of sound from confined pulsating axisymmetric jets, AIAA J. 39 (2001) 1869–1874.